

**Direct Observations of the Ionizing Star in the UC HII Region
G29.96–0.02: A Strong Constraint on the Stellar Birth Line for
Massive Stars**

Alan M. Watson

Lowell Observatory, 1400 West Mars Hill Road, Flagstaff, AZ 86001

and

Department of Astronomy, New Mexico State University, Las Cruces, NM 88001

alan@oldp.nmsu.edu

Alison L. Coil

Lowell Observatory, 1400 West Mars Hill Road, Flagstaff, AZ 86001

and

Department of Astrophysical Science, Princeton University, Peyton Hall, Princeton,

NJ 08544

alcoil@astro.princeton.edu

Debra S. Shepherd

Department of Astronomy, University of Wisconsin – Madison, 475 North Charter
Street, Madison, WI 53706

and

Radio Astronomy, California Institute of Technology, Pasadena, CA 91125

dss@milli.caltech.edu

Peter Hofner

Universität zu Köln, I. Physikalisches Institut, Zùlpicherstrasse 77, D-50937 Köln,
Germany

and

NAIC, Arecibo Observatory, PO Box 995, Arecibo, PR 00613

hofner@naic.edu

and

Ed Churchwell

Department of Astronomy, University of Wisconsin – Madison, 475 North Charter
Street, Madison, WI 53706

churchwell@astro.wisc.edu

ABSTRACT

We have observed the ultracompact HII region G29.96–0.02 in the near infrared J , H , and K bands and in the $\text{Br}\gamma$ line. By comparison with radio observations, we determine that the extinction to the nebula is $A_K = 2.14$ with a 3σ uncertainty of 0.25. We identify the ionizing star and determine its intrinsic K magnitude. The star does not have an infrared excess and so appears to be no longer accreting. The K magnitude and the bolometric luminosity allow us to place limits on the location of the ionizing star in the HR diagram. The 3σ upper limit on the effective temperature of the ionizing star is 42 500 K. We favor a luminosity appropriate for star with a mass in excess of about $60 M_\odot$. The limit on the temperature and luminosity exclude stars on the ZAMS and stars within 10^6 yr of the ZAMS. Since the age of the UC HII region is estimated to be only about 10^5 yr, we suggest that this is direct evidence that the stellar birth line for massive stars at twice solar metallicity must be significantly redder than the ZAMS.

1. Introduction

Our understanding of the formation of massive stars is primitive. In this paper, we show how observations of massive stars in ultracompact (UC) HII regions can provide information about their birth. UC HII regions are found around young massive stars still embedded in their natal molecular clouds. Statistically, the objects classified as UC HII regions by Wood & Churchwell (1989a, 1989b) appear to last for about 10–20% of the life of an O star or a few $\times 10^5$ yr. Massive stellar outflows (Harvey & Forveille 1988; Garden & Carlstrom 1992; Hunter et al. 1995; Shepherd & Churchwell 1996a, 1996b) seem to represent a still earlier and more poorly understood phase, possibly during which the massive star is still accreting.

Previously, the ionizing stars in UC HII regions have been studied through their indirect effects on the surrounding gas and dust. These studies include determinations of the bolometric luminosities (Chini et al. 1986; Wood & Churchwell 1989a), effective ionizing fluxes (Wood & Churchwell 1989a; Kurtz, Churchwell, & Wood 1994), and effective spectral hardnesses (Doherty et al. 1994). All of these methods have significant drawbacks. The bolometric luminosities are upper limits because they are determined largely from IRAS observations and most likely include contributions from luminous sources other than the ionizing star of the UC HII region. The effective ionizing flux and the effective spectral hardness are very difficult to relate to the star because of the effects of dust within the UC HII region and large uncertainties in stellar ionizing continua (see the discussion in Najarro et al. 1996).

Instead, we have chosen to observe the UC HII region G29.96–0.02 in the near infrared J , H , and K bands and in the $2.17\mu\text{m}$ $\text{Br}\gamma$ line. These observations allow direct measurements of the properties of the ionizing star. G29.96–0.02 has been previously imaged in the near infrared by Van Buren (1993), Megeath (1993), and Fey et al. (1995). These authors extracted a great deal of qualitative information from their observations and were able to make a number of suggestions. Our work builds on their work; we are able to confirm a number of their suggestions and derive important new information on the ionizing star and the nebula.

Fey et al. (1995) considered a champagne flow model for G29.96–0.02 and estimated an age for the UC HII region of about 10^5 yr from the extent of the extended radio continuum emission. Mac Low et al. (1991) and Van Buren & Mac Low (1992) modeled G29.96–0.02 as a bow shock around a star moving at $5\text{--}20\text{ km s}^{-1}$ at an angle of about 135° to our line of sight. However, the O star is closely associated with a young cluster (Fey et al. 1995 and below) and a hot core apparently containing a protostar (Cesaroni et al. 1994); this suggests that it could have moved at most 10 arcsec and so, again, has an age of less than 10^5 yr. Lumsden & Hoare (1996) found that a bow shock is a poor fit to their $\text{Br}\gamma$ velocity field and prefer instead a model similar to the one suggested by Fey et al. (1995). Mass-loaded models (Hollenbach et al. 1994; Dyson 1994; Lizano & Cantó 1995; Dyson, Williams, & Redman 1995; Redman, Williams, & Dyson 1996; Williams, Dyson, & Redman 1996; Lizano et al. 1996) can delay the expansion of an UC HII region by about 10^5 yr. If the central star was in an outflow/accretion phase before the UC HII region was created, this phase is likely to have lasted less than 10^4 yr, based on comparison with other O stars currently undergoing or just finishing molecular outflow activity (Cabrit & Bertout 1992; Shepherd & Churchwell 1996b; Acord, Walmsley, & Churchwell 1997). All of these estimates and considerations point to an age of order 10^5 yr for the UC HII region.

We adopt a heliocentric velocity of 95 km s^{-1} , the average global radio recombination line velocity (Afflerbach et al. 1994). Since G29.96–0.02 lies close to a tangent point, its distance is uncertain, and, unfortunately, the formaldehyde absorption line data of Downes et al. (1990) do not resolve the distance ambiguity. The Galactic rotation curve and error bars given by Burton (1988) yield a distance of between 5 kpc and 10 kpc.

Afflerbach, Churchwell, & Werner (1996) have determined that the abundances of O, N, and S in G29.96–0.02 are about twice those observed in the local ISM. This is consistent with its location towards the center of the galaxy.

The organization of this paper is as follows. In section 2 we present our new infrared observations. In section 3 we summarize the existing radio observations that have been kindly made available to us by a number of our colleagues. In section 4 we present the

astrometric calibration of the location of the ionizing star. In section 5 we discuss the bolometric luminosity of G29.96–0.02. In section 6 we investigate the nebula using the Br γ and radio images and derive the extinction to the nebula. In section 7 we investigate the properties of the ionizing star and its associated stellar cluster using the broad band J , H , and K images. In section 8 we summarize the principal results of this work and discuss some of their implications.

2. Infrared Data

2.1. Observations

We observed G29.96–0.02 on the night of 1995 May 21 and June 24 UT with the OSIRIS near infrared camera (Depoy et al. 1993) on the Perkins 1.8 meter telescope at Lowell Observatory. Light cirrus was present during the first night. The second night was photometric. The seeing was 1.8 arcsec FWHM on the first night and 2.0 arcsec FWHM on the second night.

OSIRIS has a 256 \times 256 NICMOS–3 detector. The re-imaging optics gave a pixel scale of 0.62 arcsec and a field of view of 150 arcsec. Images were taken through J , H , and K broad band filters and 2.12, 2.14, and 2.17 μm narrow band filters. The 2.12 μm filter includes emission from the H₂ $\nu = 0-1$ S(1) line and the 2.17 μm filter includes emission from the Br γ line; the 2.14 μm filter excludes strong emission lines.

We took several exposures through each filter, dithering the target onto each of the detector quadrants. Total exposure times in each of the broad band filters were 120 seconds on the first night and 240 seconds on the second night. Total exposure times in each of the narrow band filters were 480 seconds on the first night and 240 seconds on the second night.

2.2. Reduction

The data were reduced using custom programs within the VISTA image reduction system. Each image was corrected for non-linear response by subtracting a bias image and dividing each pixel by its estimated relative response. We have found that the non-linearity can be adequately modeled as a quadratic function and the principal variation in non-linearity in OSIRIS is between quadrants, so we determined and applied different quadratic coefficients for each quadrant. Each image was then dark subtracted, flattened, and masked to eliminate bad pixels. A single sky value was estimated for each image by fitting a quadratic to the peak of the intensity histogram and solving for the turning point. That value was then subtracted from the image.

The images were brought into a common registration by measurements of bright stars, shifted by an integral number of pixels, and co-added. This process did not noticeably degrade the seeing.

We corrected the 2.12 and 2.17 μm images for continuum emission by subtracting the 2.14 μm image after scaling by the ratio of the mean brightnesses of several stars away from the UC HII region. We did not detect any line emission in the 2.12 μm image and will not consider it further.

2.3. Broad Band Calibration

The broad band data from the second nights data were calibrated by observations of the two UKIRT faint standards 25 and 28 (Casali & Hawarden 1992). The UKIRT faint standards contain very little color information, so we did not attempt to solve a color term and have left the magnitudes on the natural system. This is less of a drawback than it seems, as our sources are so heavily reddened that color terms derived from observations of unreddened stars would be of limited use. The RMS residuals in the fits for the zero points and extinction terms were about 3%.

2.4. Narrow Band Calibration

The narrow band data from the second night was calibrated by observations of the sdO optical spectrophotometric standard BD +28 4211. This star is not an infrared spectrophotometric standard but we expect that its spectrum will be featureless in the K window. BD +28 4211 has a fainter red companion 3 arcsec to the NNW (Massey & Gronwall 1990; Thejll, Theissen, & Jimenez 1994). We measured a difference between the fainter and brighter stars of $\Delta K \approx 1.5$. Before performing photometry, we removed the companion by shifting, scaling, and subtracting a suitably centered star. We measured a K magnitude of 11.56 ± 0.04 for BD +28 4211. The absolute calibration of Bessell & Brett (1988) gives a flux of $9.62 \times 10^{-16} \text{ erg s}^{-1} \text{ cm}^{-2} \text{ \AA}^{-1}$ at 2.19 μm with a 1σ uncertainty of about 4%. Assuming a λ^{-4} spectrum, this gives a flux of $1.01 \times 10^{-15} \text{ erg s}^{-1} \text{ cm}^{-2} \text{ \AA}^{-1}$ at 2.164 μm , the peak of the 2.17 micron filter.

2.5. Infrared Images

Figure 1 presents images in J , H , K , and $\text{Br}\gamma$. The arc-shaped nebula at the center of each image is the UC HII region G29.96–0.02. The bright point source within the nebula in the J , H , and K images is the ionizing star candidate previously seen by

Van Buren (1993), Megeath (1993), and Fey et al. (1995). The position of this source is marked with a white cross in the Br γ image.

3. Radio Data

G29.96–0.02 has been extensively studied in the radio continuum, radio recombination lines, and molecular lines. We are grateful to a number of our colleagues for providing the radio images listed in Table 1 in electronic form. Table 1 lists for each image the authors, frequency, telescope, beam FWHM, and largest angular size imaged. The VLA images are all of radio continuum emission. The OVRO image is the total intensity in the C¹⁸O $J = 1 - 0$ line. We assume that the 3σ errors in the absolute flux calibration of the radio continuum images are about 20%. The errors in the C¹⁸O image are larger but do not affect our analysis.

4. Astrometry

We determined the position of the ionizing star candidate (#3 below) by cross-correlating versions of the Br γ image with the astrometrically-calibrated 1.3 and 2 cm radio continuum images. Before cross-correlating, we smoothed each pair of images to the same resolution. The ionizing star candidate is located at $\alpha_{1950} = 18\ 43\ 27.214$ and $\delta_{1950} = -02\ 42\ 35.9$ in the radio reference frame. The determinations from the 1.3 cm and 2 cm images differed by only 0.2 arcsec. The distance between the ionizing star and the peak of the 2 cm emission is 2.0 arcsec. At 5.0 kpc this corresponds to 10000 AU.

5. The Bolometric Luminosity

Table 2 lists measurements of the continuum spectral energy of G29.96–0.02. The values at 21 cm, 6 cm, and 1.3 cm were measured by us from the VLA maps obtained by Claussen & Hofner (1996), Afflerbach et al. (1994), and Cesaroni et al. (1994). The three measurements at 1.3 mm were obtained with different effective beam sizes. The measurements at 790 μm and 350 μm from Hunter (1997) may be missing extended emission. To obtain total magnitudes of $J = 12.5$, $H = 10.1$, and $K = 7.9$ for the nebula we measured the total magnitudes within a 25 arcsec box centered on the ionizing star after subtracting scaled point spread functions of all stars except the ionizing star. (We describe our photometry below.) We converted these to Jy using the flux calibration of Bessell & Brett (1988). Our measurements of $\Delta J \approx 1.9$, $\Delta H \approx 1.8$, and $\Delta K \approx 2.4$ between the flux for the ionizing star and the total flux show that nebular emission and

scattering dominate over direct light from the star even at these short wavelengths.

Figure 2 shows the spectral energy distribution plotted as $\log \nu F_\nu$ against $\log \nu$. The spectral energy distribution is characteristic of UC HII regions: optically thick free-free emission longward of a few cm, optically thin free-free emission between a few cm to about a few mm, and very strong thermal dust emission from about 1 mm to about 10 μm .

We can estimate the bolometric luminosity by integrating over the spectral energy distribution. As expected, extrapolation of the cm wavelength free-free emission to 1300 μm (the dashed line in Figure 2) indicates that the 1300 μm emission arises from hot dust. We fitted a modified Planck law $F_\nu \propto \nu^2 B_\nu(T)$ to the 1300 μm and 100 μm points, finding $T \approx 26$ K, and interpolated elsewhere. This adopted spectrum is shown by a solid line in Figure 2. We also considered the optically thick model fit by Hunter (1997); this gives a flux within 5% of ours. We derive an apparent bolometric flux of 7.00×10^{-7} $\text{erg s}^{-1} \text{cm}^{-2}$ which corresponds to an apparent bolometric magnitude of $m_{\text{bol}} = 3.90$ (where $M_{\text{bol},\odot} = 4.75$). Since this depends heavily on the IRAS 100 μm measurement, we assume a 3σ uncertainty of 30%.

Since this bolometric luminosity is integrated over an arcmin sized region, it is likely to include contributions from other sources and so is a priori only an upper limit for the bolometric luminosity of the ionizing star. However, there are no other bright sources in either the 1300 μm map of Mooney et al. (1995) or the mid infrared images of Ball et al. (1996). We do know that the IRAS beam includes both the hot core to the west of the UC HII region and a cluster of B stars apparently associated with the ionizing star (see below). Cesaroni et al. (1994) estimate that the source powering the core contributes only about 1/10 of the flux. Hofner et al. (1997) estimate that at 2.7 mm only 150 ± 50 mJy of the total 2.73 Jy arises from the hot core. Much of the total emission will be free-free emission from the UC HII region, but since the hot core does not appear in cm wavelength continuum maps we attribute its emission solely to dust. We estimate the total dust emission of the region at 2.7 mm to be about 4 Jy by extrapolating the 1.3 mm measurement of 15.6 Jy (Mooney et al. 1995) assuming a ν^2 spectrum. Thus, the hot core contributes less than 10% of the 2.7 mm dust emission. We expect that the hot core has a spectrum that is no hotter than the UC HII region and so this fraction is an upper limit to its total contribution to the bolometric luminosity. Furthermore, as we shall see below, the cluster appears to be very much less luminous than the ionizing star. This suggests that the true bolometric luminosity of the ionizing star is likely to be quite close to the total bolometric luminosity of the region. We will conservatively assume that at least half of the measured luminosity must come from the ionizing star, that is $3.90 \leq m_{\text{bol}} \leq 4.65$ with a 3σ uncertainty on the limits of 0.3.

6. The Nebula

6.1. Emission Measure and Electron Temperature

In order to predict the intrinsic flux in Br γ , we need to know both the emission measure and the electron temperature in the nebula. We can use the 2 cm, 6 cm, and 21 cm radio continuum images to provide this information. The familiar expression for the brightness temperature T_b at a given frequency ν is

$$T_b = T_e(1 - e^{-\tau}). \quad (1)$$

The optical depth is given by

$$\tau = 8.235 \times 10^{-2} a T_e^{-1.35} (\nu/\text{GHz})^{-2.1} (E/\text{cm}^{-6} \text{ pc}) \quad (2)$$

where E is the emission measure and a is a weak function of ν and T_e (Mezger & Henderson 1967). The peak synthesized beam brightness temperature measured in the 2 cm image is about 1500 K. Anticipating our result that T_e is about 6000 K and assuming that there is no unresolved structure in the 2 cm image, equation 1 implies that the peak optical depths at 2 cm, 6 cm, and 21 cm are about 0.3, 3, and 40. Thus, the 6 cm and 21 cm images provide information on different regions of the nebula. Since the dependence of a on T_e is so weak, we again anticipate our result and use its value at 6000 K.

We smoothed the 2 cm image to match the resolution of the 6 cm and 21 cm images and then calculated T_e and E iteratively. We started with an initial guess for T_e of 6000 K. We then used the 2 cm image and equations 1 and 2 to predict the 6 cm or 21 cm image. Half of the ratio between the predicted and actual 6 cm or 21 cm image was used at each point in the image as a correction factor for the value of T_e . We repeated the prediction/correction step until T_e no longer changed significantly. Images of T_b and T_e are shown in Figure 3. The effects of increasing optical depth at longer wavelength are apparent as increases in T_b and a severe reduction in contrast in the 21 cm T_b image compared to the 2 cm T_b image. In the optically thick part of the nebula, T_e is determined largely by the brightness temperature in the longer wavelength image and so has a systematic 3σ error of about 20%. In the optically thin parts of the nebula, it is difficult to separate the product of T_e and E and the errors in T_e are much larger. Random errors from imperfect imaging are more difficult to judge. The hot regions along the NW and SW of the arc in Figure 3c and the ‘bumps’ in Figure 3f are almost certainly artifacts. Ignoring these, T_e is between 5000 K and 7000 K over the bright part of the nebula, including the arc, and might possibly be about 1000 K cooler in the tail to the NE. In our following analysis we will adopt a uniform temperature of 6000 K and consider temperature variations in our discussion.

Afflerbach et al. (1994) examined the nebular properties by a non-LTE analysis of radio recombination lines. They derived T_e in the range 6200–8600 K, although with large errors. Thus, our measurement of T_e of about 6000 K is in rough agreement.

6.2. The Extinction To The Nebula

Figure 4a shows our Br γ image of G29.96–0.02. The total Br γ flux in Figure 4 is $8.42 \times 10^{-12} \text{ erg s}^{-1} \text{ cm}^{-2}$ with a 3σ uncertainty of about 12%. We measure $2.23 \times 10^{-12} \text{ erg s}^{-1} \text{ cm}^{-2}$ in a 5 arcsec aperture centered on the peak of the Br γ emission, consistent with the flux of $2.49 \times 10^{-12} \text{ erg s}^{-1} \text{ cm}^{-2}$ measured by Doherty et al. (1994), and $6.6 \times 10^{-12} \text{ erg s}^{-1} \text{ cm}^{-2}$ in a 17 arcsec aperture, consistent with the flux of $7.6 \pm 1.0 \times 10^{-12} \text{ erg s}^{-1} \text{ cm}^{-2}$ measured by Herter et al. (1981).

Figure 4b shows the 2 cm image of Fey et al. (1995) at its full resolution and Figure 4c shows it smoothed to the 1.8 arcsec FWHM resolution of our Br γ image. As we described above, the alignment of the 2 cm image was determined by cross-correlation with the Br γ image, after smoothing the 2 cm image to match the resolution of the Br γ image. The total 2 cm flux density in Figure 4 is 4.6 Jy. Fey et al. (1995) quote a flux of 3.9 Jy for the whole image, but this includes large regions with small, negative flux. The similarities between the Br γ and 2 cm images are striking; both show the strong arc of emission that lead Wood & Churchwell (1989a) to classify G29.96–0.02 as a cometary UC HII region and both show emission behind the arc and in extensions to the south east and the north. The importance of this is that it demonstrates that the emission occurs at similar optical depths and so the extended emission noted by Fey et al. (1995) is directly associated with the UC HII region rather than being a chance superposition of foreground or background emission.

We now derive a relation between the 2 cm brightness temperature and the intrinsic flux in Br γ , with the purpose of comparing the intrinsic Br γ flux to the observed Br γ flux to derive the apparent extinction at Br γ . Unless otherwise noted, all units are cgs. From equations 1 and 2, the emission measure E in cm^{-5} is

$$E = 4.72 a_{2\text{cm}}^{-1} T_e^{1.35} \nu_{2\text{cm}}^{2.1} \ln \left(\frac{T_e}{T_e - T_b} \right). \quad (3)$$

The Br γ flux $S_{\text{Br}\gamma}$ from a region of solid angle Ω is

$$S_{\text{Br}\gamma} = 0.9 h \nu_{\text{Br}\gamma} \alpha_{\text{Br}\gamma}^{\text{eff}} \frac{\Omega}{4\pi} E. \quad (4)$$

The factor of 0.9 arises because we have assumed that the nebula consists of 10% singly ionized helium by number; the ionized helium will contribute electrons and ions to the radio continuum emission but only electrons to the Br γ emission. Over the range of

temperatures of interest here, Hummer & Storey (1987) give

$$\alpha_{\text{Br}\gamma}^{\text{eff}} = 6.48 \times 10^{-11} T_e^{-1.06}. \quad (5)$$

We ignore variations of $\alpha_{\text{Br}\gamma}^{\text{eff}}$ with density as they amount to less than 1% over the range of interest here. Combining equations 3, 4, and 5 and replacing $a_{2\text{cm}}$ and $\nu_{2\text{cm}}$ gives

$$S_{\text{Br}\gamma} = 0.612 \frac{\Omega}{4\pi} T_e^{0.29} \ln \left(\frac{T_e}{T_e - T_b} \right). \quad (6)$$

To understand the errors it is worth making the approximation that $T_b \ll T_e$. The peak synthesized beam brightness temperature in the 2 cm image is only 1500 K, so this is a good approximation to first order. We then have

$$S_{\text{Br}\gamma} \approx 0.612 \frac{\Omega}{4\pi} T_e^{-0.71} T_b. \quad (7)$$

It can be seen that the 20% 3σ systematic uncertainty in T_b and T_e and the 12% 3σ uncertainty in the observed flux in Br γ translate to a 27% 3σ systematic uncertainty in the extinction.

We used equation 6 to estimate the intrinsic flux of Br γ at each point from the 2 cm image. The total intrinsic flux in Figure 4 is expected to be $6.72 \times 10^{-11} \text{ erg s}^{-1} \text{ cm}^{-2}$ and so the apparent extinction at Br γ is 2.26 mag. This extinction is an average over the whole nebula and we quote it only for illustrative purposes; we compute images of apparent extinction below.

The apparent extinction to the nebula is not uniform. Figure 4d shows an image of the apparent extinction. The apparent extinction is higher in the arc and towards the end of the extension to the south east, reaching about 2.6 mag. In the region behind the arc, in the vicinity of the ionizing star, the apparent extinction drops to about 2.20 mag, although there is some noise from continuum subtraction. The peak-to-valley contrast in the main part of the nebula is about 0.6 mag or a factor of about 1.7. It seems significant that the two regions of highest apparent extinction correspond to the two brightest regions. We can think of six possible explanations for the correlation of higher apparent extinction with surface brightness: an error in the 2 cm map, the presence of dense ionized regions in the nebula, variations in electron temperature within the nebula, variations in external extinction, a molecular sheath, and internal extinction. We consider these in turn.

(i) Errors in the 2 cm image. The kind of error in the 2 cm image that would explain the structure would have the characteristic of placing almost twice as much flux in small scale structures (the arc) than large scale structures (the tail). Since the 2 cm image is constructed from images in three VLA configurations, such an error might have

occurred if there were relative flux errors between the observations. To investigate this, we compared the 2 cm image to the 1.3 cm image. The peak optical depth in the 2 cm image is 0.3 and so optical depth effects will be important at the 10% level in the arc. Correcting both images for optical depth effects is complicated, since they have different intrinsic resolutions. Therefore, we compare the real 1.3 cm image to the prediction from the 2 cm image, obtained by assuming $T_e = 6000$ K, using equations 1 and 2 to account for optical depth and frequency effects, and smoothing from the resolution of the 2 cm image to that of the 1.3 cm image. Figure 5a and b show the observed and predicted 1.3 cm images. The predicted image has only 87% of the flux in the observed image, but this is not unexpected. Although there are significant variations in the ratio, they are only at the 10% level and are not in the sense required to explain the additional apparent extinction (the arc does not appear brighter in the 2 cm image than the 1.3 cm image). It would appear, then, that errors in the 2 cm image cannot explain the variations in apparent extinction.

(ii) Dense Ionized Regions. Our procedure above accounts for optical depth effects as long as there is no unresolved structure. It is possible, though, that unresolved dense ionized regions exist in the nebula. These would contribute strongly to $\text{Br}\gamma$ but might well be optically thick at 2 cm and contribute only weakly. However, in order to mimic the variations in the apparent extinction image, these clumps would have to avoid the brightest regions in the nebula. This seems somewhat unlikely.

(iii) Variations in Electron Temperature. As equation 7 shows, the $\text{Br}\gamma$ flux depends on the electron temperature roughly as $T_e^{-0.71}$. Thus, we could explain the factor of 1.7 peak-to-valley contrast in the ratio by a factor of 2 peak-to-valley contrast in the temperature, in the sense that the brighter regions are cooler. However, in our investigation of T_e above we discovered that this was not the case: the region around the arc is certainly not cooler than the tail and is perhaps 1000 K or 15% hotter.

(iv) Variations in External Extinction. At first glance, variable external extinction to the nebula seems a likely candidate. Figure 6 shows that G29.96–0.02 is superposed on a molecular clump with a dense core in front of the arc. However, the contours of molecular gas do not match the details of the variation in extinction: they would suggest a smooth gradient across the nebula rather than the strong correlation with nebular emission that we observe.

(v) A Molecular Sheath. The bow shock model predicts a compressed molecular sheath around the arc. Van Buren and Mac Low (1992) used the radio recombination line observation of Wood & Churchwell (1991) to show that the velocity field implied a viewing angle of about 135° in the bow shock model, i.e., the head is more distance than the tail. Nevertheless, it is possible that we are viewing the edge-brightened arc at an oblique angle through such a sheath.

We can estimate the column density through such a sheath by adopting $A_V/N_H = 1.0 \times 10^{-21} \text{ mag cm}^{-2}$ and $A_{\text{Br}\gamma}/A_V = 0.125$ (for the $R_V = 5.0$ extinction law of Cardelli, Clayton, & Mathis 1989). Our value of A_V/N_H is twice the local value to account for the higher metallicity in G29.96–0.02. We take the local average from Bohlin, Savage, & Drake (1978), although Cardelli, Clayton, & Mathis (1989) give reasons for believing that the value may be lower in molecular clouds. The excess $A_{\text{Br}\gamma}$ of about 0.4 mag corresponds to N_{H_2} of about $1.6 \times 10^{21} \text{ cm}^{-2}$. This column is similar to the predictions of $N_{\text{H}_2} \approx 5 \times 10^{21} \text{ cm}^{-2}$ for the column density through the shell in the vicinity of the stagnation point (Van Buren et al. 1990; Van Buren & Mac Low 1992), although the comparison is simplistic because we ignore the effects of geometry.

(vi) Internal Extinction. Internal extinction would provide a natural explanation of the correlation between excess apparent extinction and nebular emission. We can eliminate radiation transfer effects in hydrogen by noting that the peak emission measure in the 2 cm image is $1.4 \times 10^8 \text{ cm}^{-6} \text{ pc}$ and thus the line center optical depth in Br γ is less than 3×10^{-7} (Hummer & Storey 1987). However, dust may provide significant opacity. We can investigate this by assuming that dust is evenly mixed with a uniform density ionized gas in the nebula. We ignore the effects of scattering, which may be a better approximation than might be supposed, since the arc is most likely to be a sheet in which scattering will effectively remove photons from the line of sight. In this model, the internal extinction is

$$A'_{\text{Br}\gamma} = 0.5 (A_{\text{Br}\gamma}/A_V) (A_V/N_H) N_H \quad (8)$$

The factor of 0.5 arises because the effective optical depth of an evenly mixed slab of emitting matter is $-\ln \int_0^1 e^{-\tau l} dl = -\ln((1 - e^{-\tau})/\tau) = \tau/2 + O(\tau^2)$. If the nebula is uniform, then $N_H = EM/n_e$ and we can derive N_H from the 2 cm image and the electron density of $6 \times 10^4 \text{ cm}^{-3}$ (the average of the values from regions A, B, and W from Afflerbach et al. 1994). The peak emission measure in the full-resolution 2 cm image is $1.4 \times 10^8 \text{ cm}^{-6} \text{ pc}$ and so this model predicts a peak effective internal extinction of 0.41 magnitudes. However, the extinction must be weighted by the emission and smoothed before it can be directly compared to the Br γ map. When this is done, the peak effective internal extinction drops to 0.27. The emission-weighted value of $A'_{\text{Br}\gamma}$ is shown in Figure 7a. Figure 7b shows $A_{\text{Br}\gamma} - A'_{\text{Br}\gamma}$, the apparent extinction after subtracting the model internal extinction. The pattern of higher apparent extinction is markedly reduced in the vicinity of the arc but is not eliminated. Figure 7c shows $A_{\text{Br}\gamma} - 2A'_{\text{Br}\gamma}$, the apparent extinction after subtracting twice the model internal extinction. This almost completely removes the traces of non-uniform extinction over the majority of the nebula. A number of things could act to raise the internal extinction above our model. We could have underestimated A_V/N_H by a factor of two, but this seems unlikely (Cardelli, Clayton, & Mathis 1989). It seems more likely that the nebula is not uniform in density but includes relatively dense ionized regions with $n_e \sim 10^5 \text{ cm}^{-3}$

that contribute to both the emission and extinction along with either lower density ionized regions or neutral regions that only contribute to the extinction.

Ultimately, our lack of an alternative explanation and the striking correlation between the variations in extinction and the brightness of the nebula leads us to the conclusion that we must be seeing the effects of either a molecular sheath around a bow shock or of internal extinction. That our model for internal extinction fails to predict the magnitude of the extinction by a factor of two suggests that there are lower density or neutral inclusions in the arc of the nebula with about as much column density as the dense ionized gas. This might naturally occur in models in which UC HII regions ablate dense inclusions (Dyson 1994; Lizano & Cantó 1995; Dyson, Williams, & Redman 1995; Redman, Williams, & Dyson 1996; Williams, Dyson, & Redman 1996; Lizano et al. 1996) or in which the arc arises from a photoevaporation front being driven into an inhomogeneous medium.

The location of the star slightly off the arc means that, regardless of the origin of the additional apparent extinction associated with the arc, the extinction to the ionizing star at $\text{Br}\gamma$ is 2.20 mag with a 3σ uncertainty of 0.25 mag.

7. Stellar Properties

7.1. Near Infrared Photometry

Stellar photometry in the region of the UC HII region is hindered by the strong and variable nebular background, the degree of crowding, and the extreme colors of some of the stars which cause them to be undetected in one or more of the three bands. We adopted methods to minimize these problems.

First, we performed stellar photometry on the J , H , and K images using Jon Holtzman’s very heavily modified version of DAOPHOT (Stetson 1987). One of the modifications allowed us to fit stars in the three bands simultaneously, fixing the relative positions of stars within groups but allowing the offsets between frames to vary. We carefully added stars to each group by hand and did not allow the software to delete any. We restricted ourselves to the region of common overlap between our dithered exposures, to avoid problems associated with PSF variations (McCaughrean 1993).

Second, we scaled and subtracted the $\text{Br}\gamma$ line image from each of the broad band images before performing photometry. The scaling was determined subjectively. This procedure works well, but it is not perfect. Clearly, the ratio of broad band nebular emission to $\text{Br}\gamma$ emission is not constant, presumably because of the presense of a component such as scattered light or dust emission that is not proportional to the emission measure and because of variable extinction. The effect of this procedure can

be seen in Figure 8 which shows images of the nebula in J , H , and K both before and after suppression of the nebular emission.

Our photometry depended to some degree on the scaling factors applied to the $\text{Br}\gamma$ line image. We determined this additional uncertainty by performing photometry on images for which the scaling factors had been changed by $\pm 10\%$. Since these changes produced images that were quite noticeably under- or over- subtracted, we assumed that they correspond to 3σ errors. For the ionizing star these errors amounted to a 0.01–0.02 mag contribution to the 1σ error but for the faintest stars they amounted to as much as a 0.3 mag contribution to the 1σ error.

Our first night’s data were taken under better seeing conditions than the second’s, but the second night’s data were photometric. Accordingly, we derived relative magnitudes from the first night’s data and fixed the zero point using aperture photometry of relatively isolated stars in the second night’s data.

Table 3 gives astrometry and photometry for all stars in a 1 arcmin box centered on the ionizing star that have photometric errors of less than 0.5 in K and 1.0 in both the $J-H$ and $H-K$ colors. The errors shown are 1σ . Table 3 is ordered by increasing K magnitude and includes the offsets (Δx and Δy in arcsec) from the ionizing star. The ionizing star is #3 and its close neighbor to the WSW is #4.

We measure $K = 10.36 \pm 0.04$, $J-H = 2.40 \pm 0.05$, and $H-K = 1.59 \pm 0.05$ the ionizing star. Lumsden & Hoare (1996) report $K_n = 11.2$, $J-H = 2.4$, and $H-K_n = 1.6$ with “typical errors of 0.3–0.5 mag”. Thus, their colors are in good agreement with ours but their magnitudes are about 0.8 mag fainter. We assessed the reliability of our broad band photometry in the following manner. Our $\text{Br}\gamma$ flux is in good agreement with other measurements, suggesting that our narrow band calibration is essentially correct. We measured $2.17 \mu\text{m}$ fluxes for the isolated stars #1, #2, and #6 using simple aperture photometry. These fluxes agreed with our K magnitudes to within 0.02 mag. This suggests that the our K photometry of isolated stars is essentially correct. We do not believe we could have made a 0.8 mag error in the relative magnitudes of star #3 to the others; for star #3 to be as faint as $K = 11.2$ would require it to be almost as faint as star #5 (located 14 arcsec WSW of the ionizing star in Figure 8) but it is clearly much brighter. Although we cannot offer an explanation for the disagreement between our magnitudes and those of Lumsden & Hoare, these considerations give us confidence that ours are more reliable.

Since the stars were selected by hand, completeness is not well defined. Furthermore, the completeness varies considerably between those regions far from the nebula and bright stars, where stars as faint as $J \approx 17$, $H \approx 16$, and $K \approx 15$ have 1σ errors of 0.1 and are easy to detect, to those regions close to the nebula and bright stars where similarly bright stars might easily have been missed.

Figure 9 shows color-color diagrams of stars from Table 1. Only stars with 1σ errors of less than 0.15 in K and 0.3 in both colors are shown. Figure 9a shows stars within a 30 arcsec square centered on the ionizing star and Figure 9b shows stars outside this square. In Figure 9a, the ionizing star is shown with a solid square. The error bars show 1σ errors. The dotted lines are the loci of unreddened main sequence and giant stars from Bessell & Brett (1988) and Koornneef (1983). The dashed lines are reddening vectors corresponding to $A_\lambda \propto \lambda^{-1.6}$ (lower), $\lambda^{-1.8}$ (middle), and $\lambda^{-2.0}$ (upper) extinction laws (Martin & Whittet 1990). We have assumed mean wavelengths of 1.25 μm , 1.65 μm , and 2.20 μm for the J , H , and K filters. The length of each vector corresponds to $A_{\text{Br}\gamma} = 2.20$. The quadrilateral delimits the expected colors for a hot star in the UC HII region with $A_{\text{Br}\gamma} = 2.20 \pm 0.25$ or $A_K = 2.14 \pm 0.25$. (The scaling between $A_{\text{Br}\gamma}$ and A_K does not depend significantly on the particular extinction law.) It can be seen that most of the stars have colors consistent with moderately reddened normal stars.

7.2. The Ionizing Star

Van Buren (1993), Megeath (1993), Fey et al. (1995), and Lumsden & Hoare (1996) have suggested that star #3 is the principal ionizing source of the UC HII region. Star #3 has $K = 10.36 \pm 0.04$, $J - H = 2.40 \pm 0.05$, and $H - K = 1.59 \pm 0.05$. These colors are in excellent agreement with those predicted for a hot star reddened by the measured extinction of the nebula (shown as a quadrilateral in Figure 9a). Of the stars that are candidate members of the young cluster (discussed below), #3 is the brightest, has no infrared excess, and is situated in the center of the brightest arc of nebular emission. This strongly supports the previous suggestions that it is the primary source of ionization. There is no evidence for an infrared excess at K . This suggests that any remaining disk is optically thin at temperatures of about 1300 K and so the star is no longer accreting.

We can estimate the intrinsic apparent K magnitude m_K of the ionizing star by using the extinction of $A_K = 2.14$ with a 3σ uncertainty of 0.25 and our measurement of $K = 10.36$ with a 3σ uncertainty of 0.12. We find the intrinsic m_K is 8.22 with a 3σ uncertainty of 0.28. Since the star does not have an infrared excess, we can estimate the intrinsic apparent V magnitude m_V from m_K by assuming an intrinsic $V - K$ close to -0.90 (Koornneef 1983). We find the intrinsic m_V is 7.32 with a 3σ uncertainty of 0.28. In Section 5 we determined $3.90 \leq m_{\text{bol}} \leq 4.65$ with a 3σ uncertainty on the limits of 0.3. To proceed we need to relate m_V and m_{bol} . We adopt the bolometric correction $\text{BC} \equiv m_{\text{bol}} - m_V$ given by Vacca, Garmany, & Shull (1996). (We use their equations 3 and 5 and hold the luminosity class constant at V, as the luminosity class makes very little difference.) This comes from a fit to a number of non-LTE atmospheres.

With our limits on the distance, m_V , m_{bol} , and $m_V - m_{\text{bol}}$ we can construct limits on the L_{bol} and T_{eff} of the star. The regions allowed by 1σ , 2σ and 3σ errors are shown in Figure 10 by thick solid lines. The thin dotted lines show the loci where $m_V = 7.32$ at different distances. Also shown in Figure 10 are evolutionary tracks and isochrones of the $Z = 2Z_{\odot}$ models of Meynet et al. (1994). The thin solid lines are tracks for 120, 85, 60, 40, 25, and $20M_{\odot}$ models, the thick dashed line is the zero-age main-sequence (ZAMS), and thin dashed lines are the 1, 2, 3, 4×10^6 yr isochrones. We only show the tracks on the first excursion to the red. The dashed-dotted lines are approximate example stellar birth lines. Stellar birth lines have not yet been constructed at $Z = 2Z_{\odot}$. Instead, we have applied the differences in the L_{bol} and T_{eff} between the Meynet et al. (1994) $Z = Z_{\odot}$ and $Z = 2Z_{\odot}$ ZAMS to the $Z = Z_{\odot}$ ‘case 1’ (right) and ‘case 3’ (left) models of Bernasconi & Maeder (1996). (The ‘case 1’ and ‘case 3’ models differ in their accretion rate.) This difference accounts for the change in atmospheric structure, to first order, but fails to account for the increase of the rate of evolution with metallicity (Bernasconi 1996, private communication). These birth lines are, therefore, almost certainly somewhat too blue.

It can be seen from Figure 10 that the 1, 2, and 3σ upper limits on the effective temperature of the ionizing star are 37 500, 40 000, and 42 500 K. If the ionizing star is a single star or an unequal-mass binary, our observations place a firm lower limit on its mass of about $30M_{\odot}$. If almost all of the bolometric luminosity in the region arises from the ionizing star, as we suspect, then this limit is about $60M_{\odot}$.

The ZAMS lies entirely outside the region allowed by our observations. Although equal-mass binaries are common among O stars (Garmany, Conti, & Massey 1980), a pair of binary ZAMS stars are also inconsistent with our observations. For consistency with the ZAMS, we require three ZAMS $40M_{\odot}$ stars at the minimum allowed distance and a conspiracy of 3σ errors. We examined the residual image after subtracting a scaled PSF and found no evidence for elongation. We conservatively place an upper limit on the separation of the components of such a system as half the FWHM or about 4000 AU at 5 kpc. This is much smaller than the size typical for early-type Trapezium systems (Abt 1986). The dynamical time for such a compact system is only about 10^4 yr, so it would dissolve over the estimated age of 10^5 yr unless it were formed in a stable, hierarchical state. We consider this explanation forced and extremely unlikely.

The tracks of evolved stars with ages in excess of 10^6 yr coincide with the region allowed by the data, but we reject this possibility because the age of the UC HII region is only about 10^5 yr. Since the ionizing star appears to be too cool at a given luminosity to be a ZAMS star, one might think it could be a pre-main-sequence star evolving onto the ZAMS from the Hayashi track at roughly constant L_{bol} but increasing T_{eff} . However, the modern theory of the formation of massive stars is that pre-main-sequence stars evolve almost along the ZAMS with both L_{bol} and T_{eff} increasing, although they diverge

from the ZAMS at the highest masses because of evolutionary effects (Beech & Mitalas 1994; Bernasconi & Maeder 1996). When they finish accreting, the most massive stars are somewhat cooler than the ZAMS. This locus is known as the stellar birth line. Our observations suggest that the stellar birth line at $Z = 2Z_{\odot}$ must be sufficiently red that the star could evolve from it into the region allowed by the data in only about 10^5 yr. Such a birth line must be cooler than about 40000 K at least at some point for stars more massive than about $40M_{\odot}$. Two example stellar birth lines from Bernasconi & Maeder (1996), crudely modified as described above, are shown by dashed-dotted lines in Figure 10. It can be seen that they do indeed diverge from the ZAMS sufficiently to explain the appearance of a star with an age of 10^5 yr at such low temperatures.

7.3. A Young Cluster

Fey et al. (1995) suggested that star #3 is a member of a young cluster. We are now in a good position to test this suggestion, as we know the extinction to the nebula and have good colors for the stars. Unfortunately, we cannot perform a statistical test for an overdensity of stars close to the UC HII region because completeness is so complex and poorly determined in the vicinity of the nebula.

The stars with $H-K > 1$ in Table 3 and Figure 9a are #3, #4, #13, #14, and #24. These stars are marked in Figure 11. Since they are projected close to the UC HII region and have extinctions that are similar the UC HII region, these are good candidate members of a cluster that is physically associated with the UC HII region. It is worth noting that with the exception of #3 and #14 these stars are not especially prominent in the images. By a visual inspection of the images alone, we might well have suggested that the bright stars to the NNE of star #3 were part of the cluster, but these appear to be foreground stars by virtue of their lower extinctions.

The star with the most extreme infrared excess is star #4, located only 1.9 arcsec SSW of the ionizing star. This star is difficult to see without suppressing the nebula emission (see Figure 8) and has not been previously noted. Comparing it directly to the ionizing star gives an $H-K$ excess of 0.75 with a 3σ error of 0.19. The presense of this infrared excess star and the absence of similar stars away from the nebula is further evidence both that the cluster is real and that it is young.

We estimated the spectral types of these stars from their H magnitudes as the K magnitudes of the infrared excess stars are presumably severely contaminated with emission from circumstellar dust. We scale the extinction to the nebula by a $\lambda^{-1.8}$ law and find $A_H \approx 3.6$. At a distance of 5 kpc the ionizing star #3 has $M_H \approx -5.1$ and the other stars #4, #13, #14, and #24 are much fainter with $M_H \approx -3.6, -3.0, -2.7,$ and -1.8 with uncertainties of at least half a magnitude. Cluster stars other than

the ionizing star have luminosities appropriate for early to mid B stars (Schmidt-Kaler 1982; Koornneef 1983). The situation in the cluster appears somewhat similar to that in M17 (Hanson & Conti 1995) in which naked O stars appear with enshrouded B stars, although possibly here the division between naked and enshrouded stars is not so sharp.

No stars are visible in the vicinity of the dense core located about 5 arcsec W of the ionizing star. This is consistent with the estimate of $A_K \approx 400$ through the core (Cesaroni et al. 1994).

8. Summary and Discussion

We have demonstrated that the stellar and nebular properties of UC HII regions can be studied in the near infrared using moderate integration times on moderate aperture telescopes. These observations give direct, quantitative information on the color and luminosity of the ionizing star. Additionally, they give important information on the extinction to the nebula and the pattern of dust in and around the nebula.

Our observations of G29.96–0.02 confirm that the extended radio continuum emission seen by Fey et al. (1995) is indeed associated with the bright arc of emission seen by Wood & Churchwell (1989a). This extended emission does not appear to be naturally explained by the bow shock model. Fey et al. (1995) suggest a stationary model in which the arc and the extended emission are explained by the density gradient in the molecular cloud. The extinction to the UC HII region derived from radio continuum and Br γ imaging amounts to $A_K \approx 2.25$ or $A_V \approx 25$ and is higher in the region of the arc. The most likely explanation for the additional extinction is that we are seeing a dense molecular sheath around the arc or that there is significant internal extinction. The required magnitude of the internal extinction requires roughly twice as much column density in low density or neutral gas as there is in dense ionized gas in the vicinity of the arc. This might naturally occur in models in which UC HII regions ablate dense inclusions (Dyson 1994; Lizano & Cantó 1995; Dyson, Williams, & Redman 1995; Redman, Williams, & Dyson 1996; Williams, Dyson, & Redman 1996; Lizano et al. 1996) or in which the arc arises from a photoevaporation front being driven into an inhomogeneous medium.

We confirm the identity of the ionizing star responsible for ionizing the UC HII region. It is located at the center of the arc of emission, as predicted by both the bow shock and stationary models for the morphology of the UC HII region. Direct light from the ionizing star accounts for only about 1/6 of the total light in each of the J , H , and K bands. The rest is presumably the result of thermal emission from dust, scattering from dust, and line and continuum emission from ionized gas.

The ionizing star does not possess a significant excess at K , indicating that it is no longer accreting. This also suggests that the photoevaporating disk model of Hollenbach et al. (1994) may not be applicable to G29.96–0.02 in its current state, although detailed predictions of the spectrum of such a disk are required to confirm this.

We confirm the suggestion of Fey et al. (1995) that the ionizing star is closely associated with a number of stars with luminosities appropriate for B stars. One of these stars has a strong infrared excess, confirming that the cluster is young. The lack of other luminous sources suggests that the ionizing star dominates the bolometric luminosity of the cluster and so is likely to have a mass of $60M_{\odot}$ or more.

Our measurement of the intrinsic m_K of the ionizing star, along with existing limits on the bolometric luminosity and distance, allow us to place limits on where the ionizing star can appear in the HR diagram. We find that the ionizing star is too cool to be within 10^6 yr of the ZAMS, in apparent contradiction with the age of about 10^5 yr estimated for the the UC HII region. This suggests that the stellar birth line (Beech & Mitalas 1994; Bernasconi & Maeder 1996) for G29.96–0.02 must be fairly cool: cooler than about 40000 K for some mass in excess of $40M_{\odot}$. This places an important limit on how blue the stellar birth line can be; a red limit already exists, as the stellar birth line must extend to at least about $90M_{\odot}$ (Bernasconi & Maeder 1996). The implications of such a red birth line for the accretion history cannot be judged at the moment as theoretical models have not yet been constructed at the twice solar metallicity appropriate for G29.96–0.02. We place a firm lower limit on the mass of the ionizing star at $30M_{\odot}$ but favor a mass in excess of about $60M_{\odot}$.

Our discovery that the ionizing star in G29.96–0.02 is significantly cooler than the ZAMS is a further strike against the method of determining the spectral type of the ionizing star in an UC HII region from an estimate of its ionizing continuum flux or spectral hardness. We can see this by considering the solar metallicity models of Schaerer & de Koter (1996). These models combine a stellar atmosphere code and a stellar evolution code. Their evolved $85M_{\odot}$ and $60M_{\odot}$ models with $\log T_{\text{eff}} \approx 4.6$ (models E3 and D3) have similar Lyman continuum fluxes to their ZAMS $40M_{\odot}$ and $25M_{\odot}$ models (models C1 and B1). Although these specific models have solar metallicity, we expect that similar discrepancies will arise regardless of metallicity. Attempts to use the bolometric luminosity to determine the mass of the ionizing stars in UC HII regions are in better shape, as massive stars evolve initially at almost constant L_{bol} , although source confusion remains a problem.

This work has benefited from discussions with and comments by Paulo Bernasconi, Pepe Franco, Jay Gallagher, Margaret Hanson, Lynne Hillenbrand, Melvin Hoare, Todd Hunter, Tom Megeath, & Robin Williams and from a very thorough report from an anonymous referee. We thank Jon Holtzman for access to and instruction

in the use of his simultaneous PSF-fitting photometry routines. Our observations were made using the Perkins Reflector of the Ohio Wesleyan University and the Ohio State University at the Lowell Observatory. We thank Andrew Afflerbach, Riccardo Cesaroni, Mark Claussen, Alan Fey, Ralph Gaume, and Stan Kurtz for allowing us to use their published and unpublished data. AMW and PH are grateful for partial support from NATO grant No. 960776. ALC is grateful for an NSF REU internship administered by Kathy Degioia-Eastwood and Northern Arizona University.

REFERENCES

- Abt, H. A. 1986, *ApJ*, 304, 688
- Acord, J. M., Walmsley, C. M., & Churchwell, E. 1997, *ApJ*, 473, 693
- Afflerbach, A., Churchwell, E., Hofner, P., & Kurtz, S. 1994, *ApJ*, 437, 697
- Afflerbach, A., Churchwell, E., & Werner, M. 1996, *ApJ*, submitted
- Ball, R., Meixner, M. M., Keto, E., Arens, J. F., & Jernigan, J. G. 1996, *AJ*, 112, 1645
- Beech, M., & Mitalas, R. 1994, *ApJS*, 95, 517
- Bernasconi, P. A., & Maeder, A. 1996, *A&A*, 307, 829
- Bessell, M. S. & Brett, J. M. 1988, *PASP*, 100, 1134.
- Bohlin, R. C., Savage, B. D., & Drake, J. F. 1978, *ApJ*, 224, 132
- Burton, W. B. 1988, *Galactic and Extragalactic Radio Astronomy*, ed. G.L. Verschuur & K.I. Kellermann (Berlin: Springer), 2nd edition, p. 295.
- Cabrit, S., & Bertout, C. 1992, *A&A*, 261, 274
- Cardelli, J. A., Clayton, G. C., & Mathis, J. S. 1989, *ApJ*, 345, 245
- Casali, M. M., & Hawarden, T. G. 1992, *JCMT–UKIRT Newsletter*, 3, 33
- Cesaroni, R., Churchwell, E., Hofner, P., & Walmsley, C. M. 1994, *A&A*, 288, 903
- Claussen, M. J., & Hofner, P. 1996, *BAAS*, 187, #108.08
- Chini, R., Kreysa, E., Mezger, P. G., & Gemünd, H.-P. 1996, *A&A*, 154, L8
- Depoy, D. L., Atwood, B., Byard, P. L., Frogel, J., & O'Brien, T. P. 1993, *Proc. SPIE*, 1946, 667
- Doherty, R. M., Puxley, P., Doyon, R., & Brand, P. W. J. L. 1994, *MNRAS*, 266, 497
- Downes, D., Wilson, T. L., Bieging, J., & Wink, J. 1980, *A&A* 40, 379
- Dyson, J. E. 1994, in *Star Formation Techniques in Infrared and mm-wave Astronomy*, ed. T. P. Ray & S. V. Beckwith (Berlin: Springer), p. 93
- Dyson, J. E., Williams, R. J. R., & Redman, M. P. 1995, *MNRAS*, 277, 700

- Fey, A. L., Gaume, R. A., Claussen, M. J., & Vrba, F. J. 1995, *ApJ*, 453, 308
- Garden, R. P., & Carlstrom, J. E. 1992, *ApJ*, 392, 602
- Garmany, C. D., Conti, P. S., & Massey, P. 1980, *ApJ*, 242, 1063
- Hanson, M. M., & Conti, P. S. 1995, *ApJ*, 448, L45
- Harvey, P. M., & Forveille, T. 1988, *A&A*, 197, L19
- Hertner, T., Helfer, H. L., Forrest, W. J., McCarthy, J., Houck, J. R., Willner, S. P., Puetter, R. C., Rudy, R. J., Soifer, B. T. & Pipher, J. L. 1981, *ApJ*, 250, 186
- Hofner, P., Kurtz, S., Churchwell, E., & Watson, A. M. 1996, *BAAS*, 188, 17.07
- Hofner, P., & Churchwell, E. 1993, in *Astrophysical Masers*, eds. A. W. Clegg & G. E. Nedoluha (Springer, Berlin), p. 164
- Hollenbach, D., Johnstone, D., Lizano, S., & Shu, F. 1994, *ApJ*, 428, 654
- Hummer, D. G., & Storey, P. J. 1987, *MNRAS*, 224, 801
- Hunter, T. R. 1997, Ph.D. Thesis, California Institute of Technology
- Hunter, T. R., Testi, L., Taylor, G. B., Tofani, G., Felli, M., Phillips, T. G. 1995, *A&A*, 302, 249
- Kurtz, S., Churchwell, E., & Wood, D. O. S. 1994, *ApJS*, 91, 659
- Koornneef, J. 1983, *A&A*, 128, 84
- Lizano, S., & Cantó, J. 1995, in *Circumstellar Disks, Outflows, and Star Formation*, ed. S. Lizano & J. M. Torrelles, *Rev. Mex. Astron. Astrofis. Ser. Conf.*, 1, 29
- Lizano, S., Cantó, J., Garay, G., & Hollenbach, D. 1996, *ApJ*, 468, 739
- Lumsden, S. L., & Hoare, M. G. 1996, *ApJ*, 464, 272
- Mac Low, M.-M., Van Buren, D., Wood, D. O. S., & Churchwell, E. 1991, *ApJ*, 369, 395.
- Martin, P. G., & Whittet, D. C. B. 1990, *ApJ*, 357, 113
- Massey, P., & Gronwall, C. 1990, *ApJ*, 358, 344
- McCaughrean, M. J. 1993, in *Massive Stars: Their Lives in the Interstellar Medium*, eds. J. P. Cassinelli & E. Churchwell (San Francisco: ASP), p. 80
- Megeath, S. T. 1993, private communication
- Meynet, G., Maeder, A., Schaller, G., Schaerer, D., & Charbonnel, C. 1994, *A&AS*, 103, 97
- Mezger, P. G., & Henderson, A. P. 1967, *ApJ*, 147, 471
- Mooney, T., Sievers, A., Mezger, P. G., Solomon, P. M., Kreysa, E., Haslam, C. G. T., & Lemke, R. 1995, *A&A*, 299, 869

- Najarro, F., Kudritzki, R. P., Cassinelli, J. P., Stahl, O., & Hillier, D. J. 1996, *A&A*, 306, 892
- Pratap, P., Menten, K. M., & Snyder, L. E. 1994, *ApJ*, 430, L129
- Redman, M. P., Williams, R. J. R., & Dyson, J. E. 1996, *MNRAS*, 280, 661
- Schaerer, D., & de Koter, A. 1996, *A&A*, submitted
- Schmidt-Kaler, T. 1982, in *Landolt-Börstein, New Series, Group VI, Vol. 2*, ed. K. Schaifers & H. H. Voigt (Berlin: Springer), p. 1
- Shepherd, D. S., & Churchwell, E. 1996a, *ApJ*, 457, 267
- Shepherd, D. S., & Churchwell, E. 1996b, *ApJ*, 472, 225
- Stetson, P. B. 1987, *PASP*, 99, 191
- Thejll, P., Theissen, A., & Jimenez, R. 1994, *A&A*, 292, 457
- Vacca, W. D., Garmany, C. D., & Shull, J. M. 1996, *ApJ*, 460, 914
- Van Buren, D. 1993, in *Massive Stars: Their Lives in the Interstellar Medium*, ed. J. P. Cassinelli & E. Churchwell, (San Francisco: ASP), p. 315
- Van Buren, D. & Mac Low, M.-M. 1992, *ApJ*, 394, 534.
- Van Buren, D., Mac Low, M.-M., Wood, D. O. S., & Churchwell, E. 1990, *ApJ*, 353, 570
- Williams, R. J. R., Dyson, J. E., & Redman, M. P. 1996, *MNRAS*, 280, 667
- Wood, D. O. S., & Churchwell, E. 1989a, *ApJS*, 69, 831
- Wood, D. O. S., & Churchwell, E. 1989b, *ApJ*, 340, 265
- Wood, D. O. S., & Churchwell, E. 1991, *ApJ*, 372, 199
- Wood, D. O. S., Handa, T., Kukua, Y., Churchwell, E., Sofue, Y., & Iwata, T. 1988, *ApJ*, 326, 884

Figure Captions

Fig. 1.— A 60×60 arcsec region around G29.96–0.02. The axes are marked in arcsec north and west of the ionizing star. Darker shades indicate brighter emission. (a) J band. (b) H band. (c) K band. (d) $\text{Br}\gamma$ with a white cross marking the location of the ionizing star.

Fig. 2.— The spectral energy distribution for G29.96–0.02. The points are taken from Table 2. The dashed line is a $\nu^{0.1}$ extrapolation from the 2 cm measurement and shows that optically thin free-free emission dominates to about 2 mm. The dotted line is a ν^4 extrapolation from the 1300 μm measurement and shows that the sub-mm region is dominated by optically thin thermal dust emission. The solid line below 100 μm is a fit to $\nu^2 B_\nu(T)$ which gives $T = 26$ K. The solid line above 100 μm is a linear interpolation in $(\log F_\nu, \log \nu)$.

Fig. 3.— A 30×30 arcsec region around G29.96–0.02. In each panel, the white cross marks the location of the ionizing star, the axes are marked in arcsec north and west of the star, and the beam size is marked in the lower left. Darker shades indicate higher temperatures. (a) The brightness temperature T_b at 2 cm smoothed to the resolution of the 6 cm image. The contours are at 25, 50, 100, 200, 400, and 800 K. (b) The brightness temperature T_b at 6 cm. The contours are at 250, 500, 1000, 2000, and 4000 K. (c) The electron temperature T_e derived from the 2 cm and 6 cm images. The contours are at 4000, 5000, 6000, and 7000 K. (d) The brightness temperature T_b at 2 cm smoothed to the resolution of the 21 cm image. The contours are at 25, 50, 100, 200, 400, and 800 K. (e) The brightness temperature T_b at 21 cm. The contours are at 500, 1000, 2000, and 4000 K. (c) The electron temperature T_e derived from the 2 cm and 21 cm images. The contours are at 4000, 5000, 6000, and 7000 K.

Fig. 4.— A 30×30 arcsec region around G29.96–0.02. In each panel, the white cross marks the location of the ionizing star, the axes are marked in arcsec north and west of the star, and the beam size is marked in the lower left. Darker shades indicate higher values. (a) The observed flux in $\text{Br}\gamma$. The contours are spaced by factors of two. (b) The observed flux in 2 cm radio continuum at full resolution. The contours are spaced by factors of two. (c) The observed flux in 2 cm radio continuum smoothed to match the resolution of the $\text{Br}\gamma$ image. The contours are spaced by factors of two. (d) The apparent extinction at $\text{Br}\gamma$. The contours are at 1.8, 2.0, 2.2, 2.4, and 2.6.

Fig. 5.— A 30×30 arcsec region around G29.96–0.02. In each panel, the white cross marks the location of the ionizing star, the axes are marked in arcsec north and west of the star, and the beam size is marked in the lower left. Darker shades indicate higher values. (a) The observed flux at 1.3 cm. The contours are spaced by factors of two. (b) The predicted flux at 1.3 cm from the 2 cm image. The contours are spaced by

factors of two and have the same values as in (a). (f) The ratio of the observed flux to the predicted flux at 1.3 cm. The contours are at 0.8, 0.85, and 0.9

Fig. 6.— A 30×30 arcsec region around G29.96–0.02. In each panel, the white cross marks the location of the ionizing star, the axes are marked in arcsec north and west of the star, and the beam size is marked in the lower left. Darker shades indicate higher values. (a) The total line flux in C^{18}O . The contours are spaced by factors of two. Negative contours are dashed. The white circle marks the FWHM 4 arcsec ammonia clump seen by Cesaroni et al. (1994). The white crosses (\times) mark the locations of the water masers seen by Hofner & Churchwell (1993). The white square (\square) marks the locations of the formaldehyde maser seen by Pratap, Menten, & Snyder (1994). (b) The apparent extinction at $\text{Br}\gamma$. The contours are at 1.8, 2.0, 2.2, 2.4, and 2.6. The C^{18}O contours from (a) are superposed.

Fig. 7.— A 30×30 arcsec region around G29.96–0.02. In each panel, the white cross marks the location of the ionizing star, the axes are marked in arcsec north and west of the star, and the beam size is marked in the lower left. Darker shades indicate higher values. (a) The model internal extinction at $\text{Br}\gamma$. The contours are at 0.05, 0.10, 0.15, 0.20, and 0.25. (b) The apparent external extinction after removing the model internal extinction. The contours are at 1.8, 2.0, 2.2, 2.4, and 2.6. (c) The apparent external extinction after removing twice times the model internal extinction. The contours are at 1.8, 2.0, 2.2, 2.4, and 2.6.

Fig. 8.— A 60×60 arcsec region around G29.96–0.02. Darker shades indicate brighter emission. (a) J band. (b) J band with nebular emission suppressed. (c) H band. (d) H band with nebular emission suppressed. (e) K band. (f) K band with nebular emission suppressed.

Fig. 9.— (a) Color-color diagram for stars within a 30 arcsec square centered on the ionizing star. (b) Color-color diagrams for stars outside that box. The error bars are 1σ . Only stars with 1σ errors of less than 0.15 in K and 0.3 in both colors are shown. The ionizing star is marked with a solid symbol. The dotted lines are the loci of main-sequence and giant stars. The dashed lines are reddening vectors of $\lambda^{-1.6}$, $\lambda^{-1.8}$, and $\lambda^{-2.0}$ reddening laws and correspond to $A_{\text{Br}\gamma} = 2.20$. The quadrilateral shows the expected colors of a hot star with $A_{\text{Br}\gamma} = 2.20 \pm 0.25$ under these reddening laws.

Fig. 10.— A theoretical HR diagram. The region allowed by 1σ , 2σ , and 3σ uncertainties on the measured properties of the ionizing star are shown by thick solid lines. The thin dotted lines show the loci where $m_V = 7.32$ at different distances. Also shown are tracks and isochrones of the $Z = 2Z_\odot$ models of Meynet et al. (1994). The solid lines are tracks for 120, 85, 60, 40, 25, and $20M_\odot$ models, the dashed lines are the zero-age main-sequence (ZAMS), and 1, 2, 3, 4×10^6 yr isochrones. The dashed-dotted

lines are approximate stellar birth lines. As described in the text, these birthlines are almost certainly somewhat too blue.

Fig. 11.— (a) A 30×30 arcsec region around G29.96–0.02 showing the K band emission. Darker shades indicate brighter emission. Candidate members of a cluster associated with the UC HII region are marked. (b) As (a) but with nebular emission suppressed.

Fig. 1

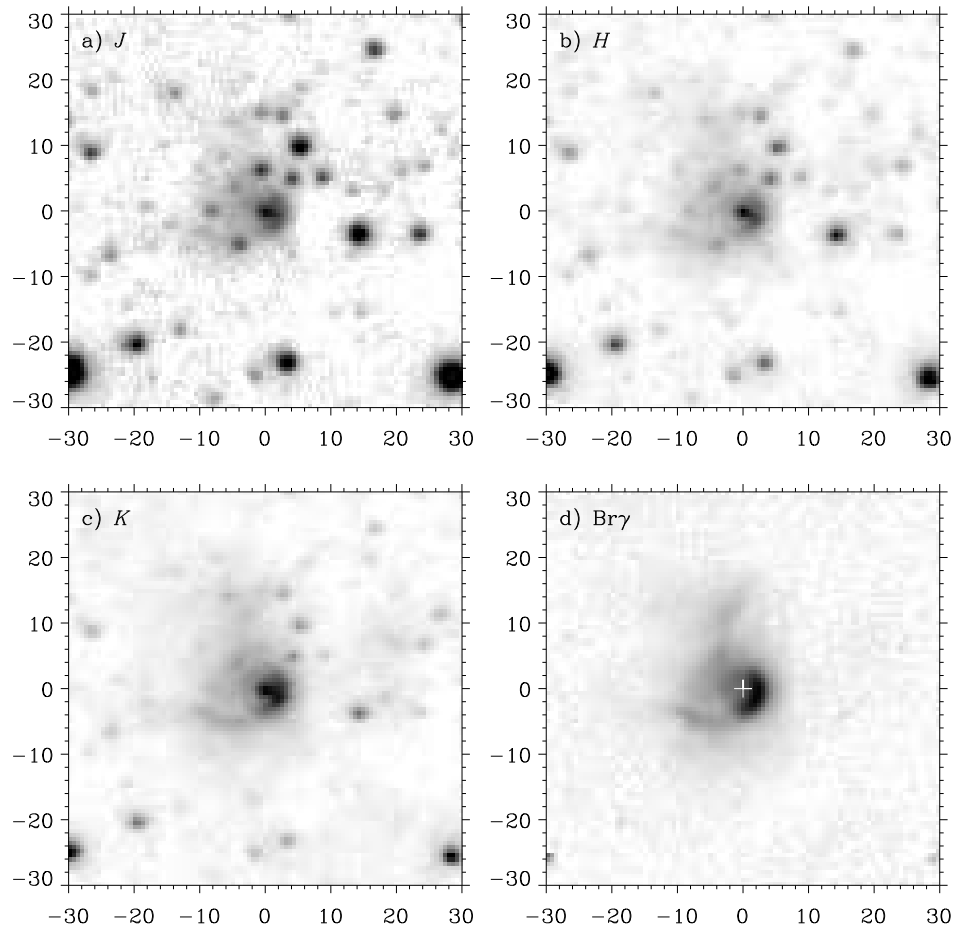


Fig. 2

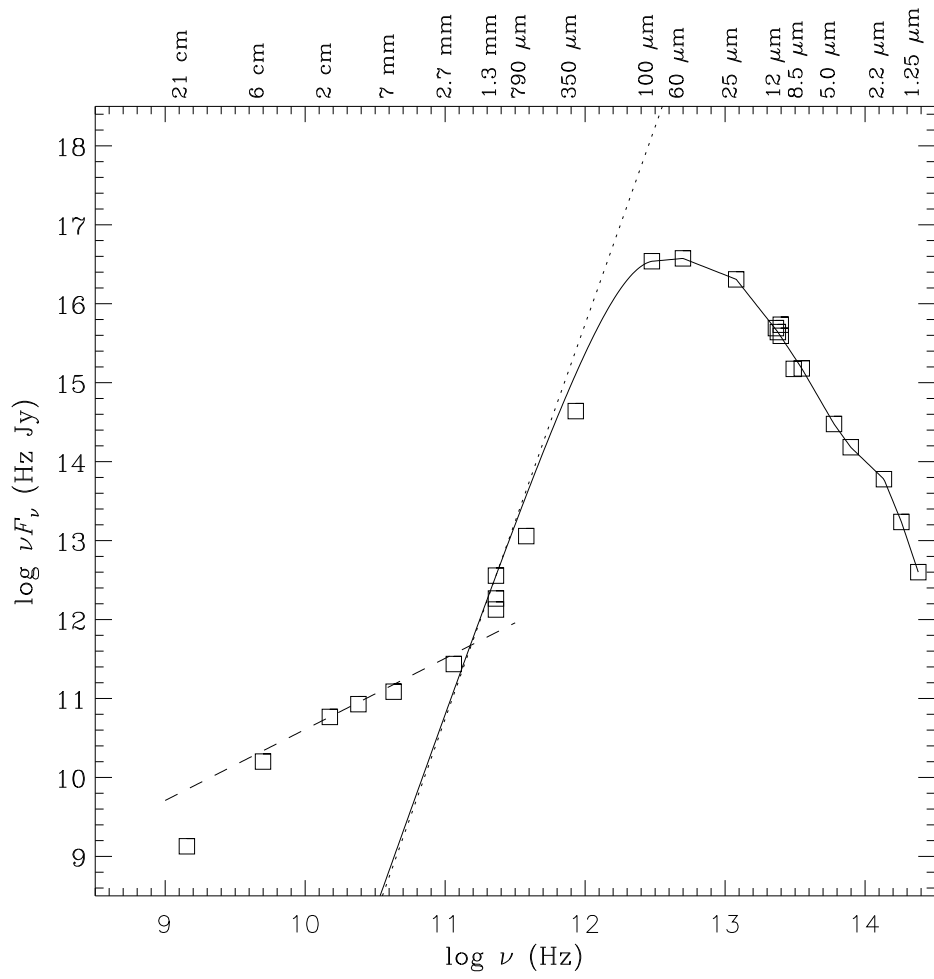


Fig. 3

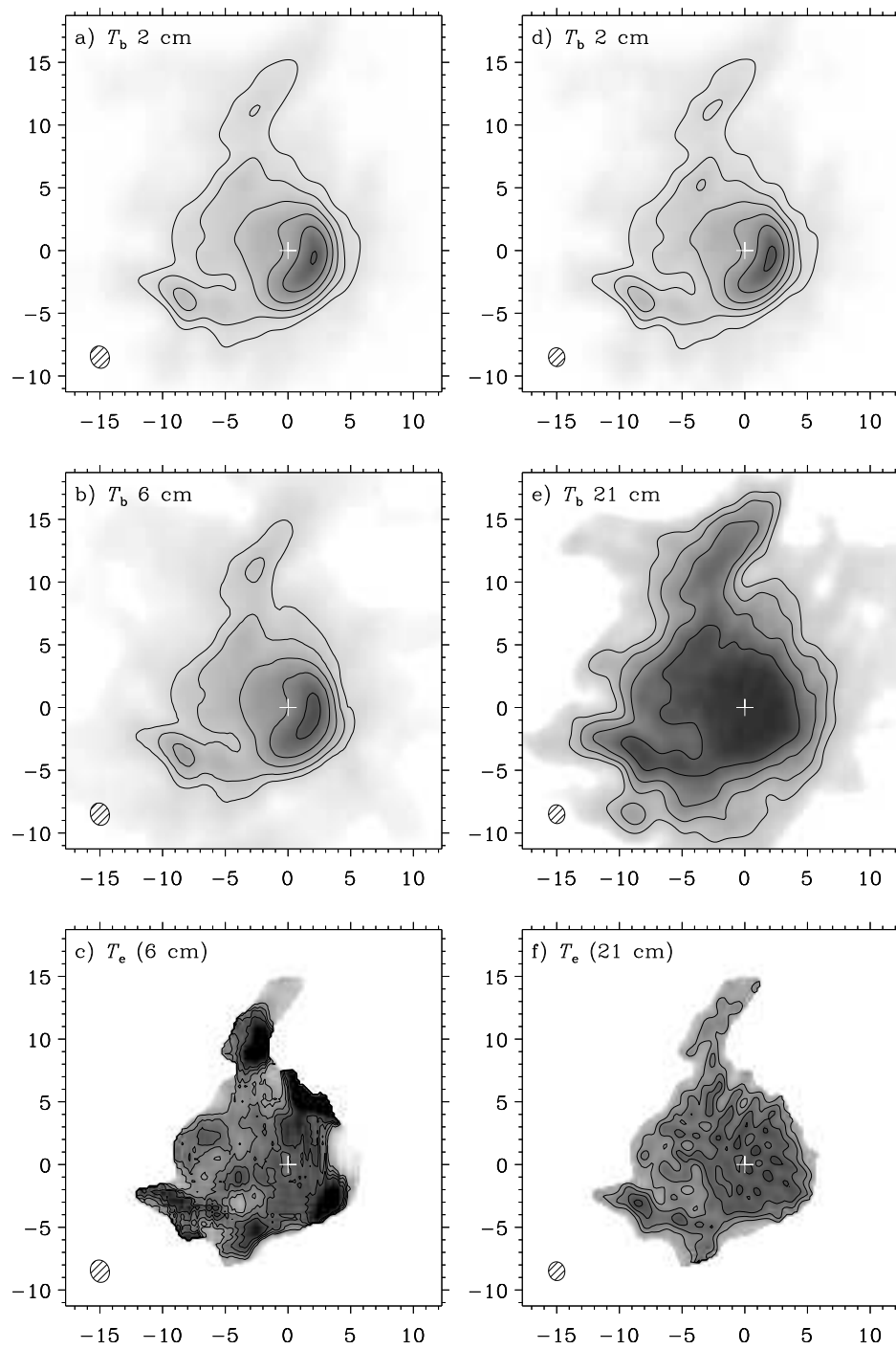


Fig. 4

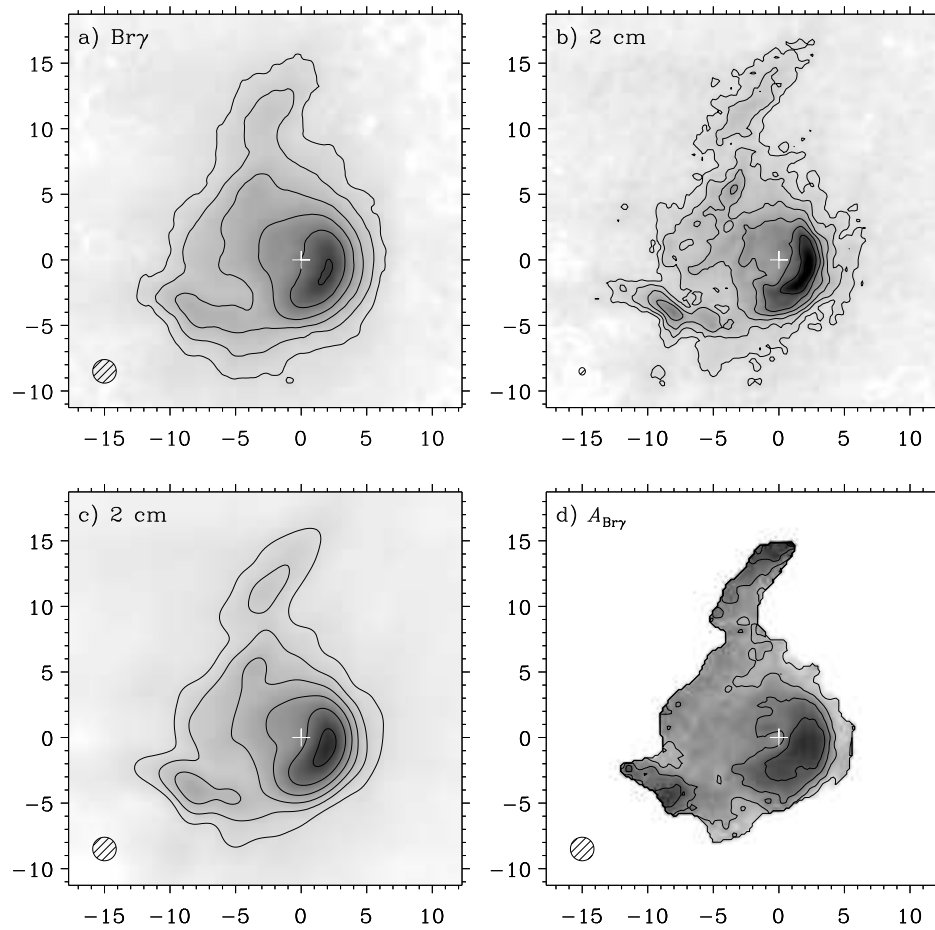


Fig. 5

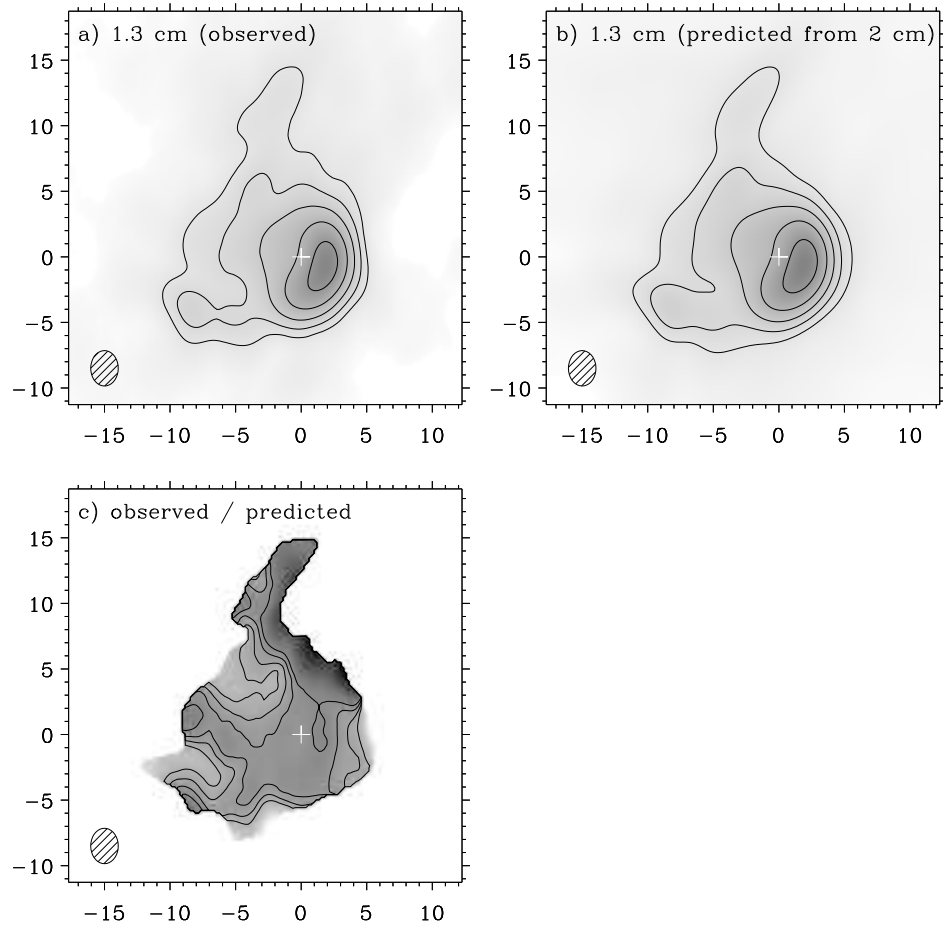


Fig. 6

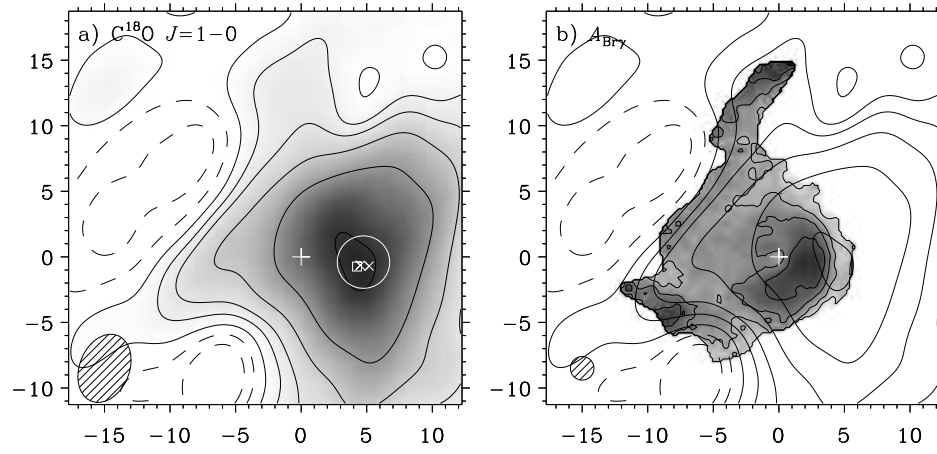


Fig. 7

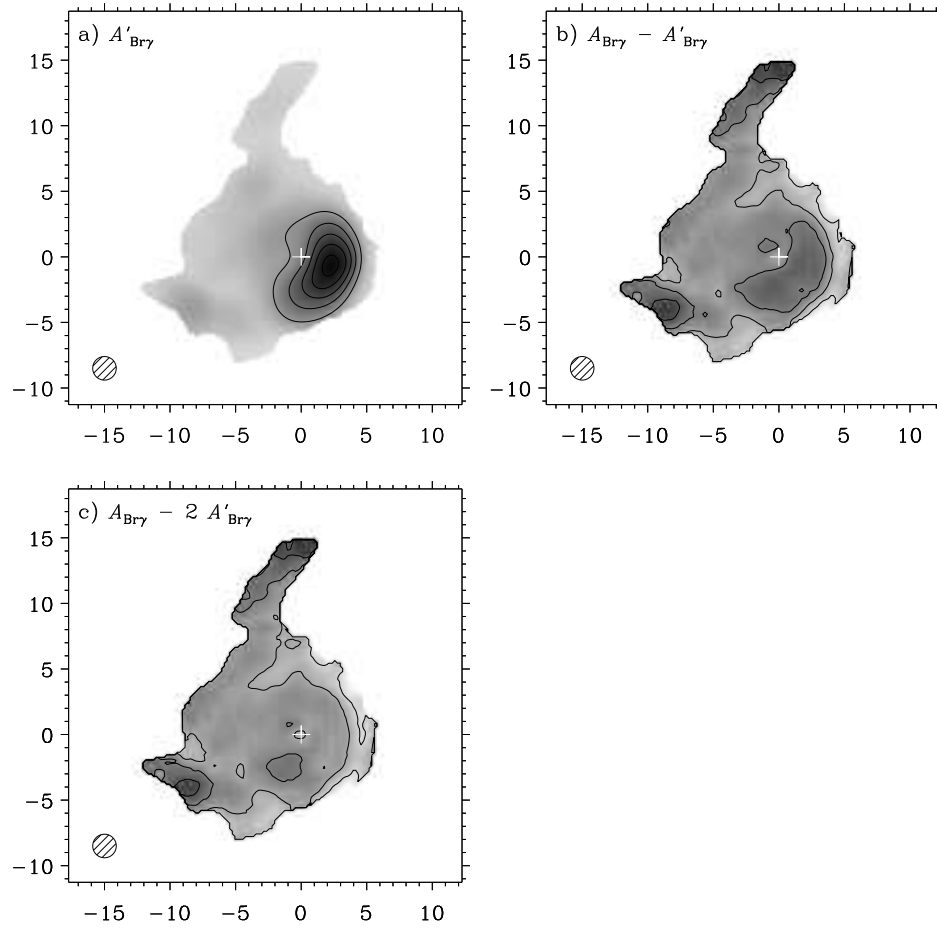


Fig. 8

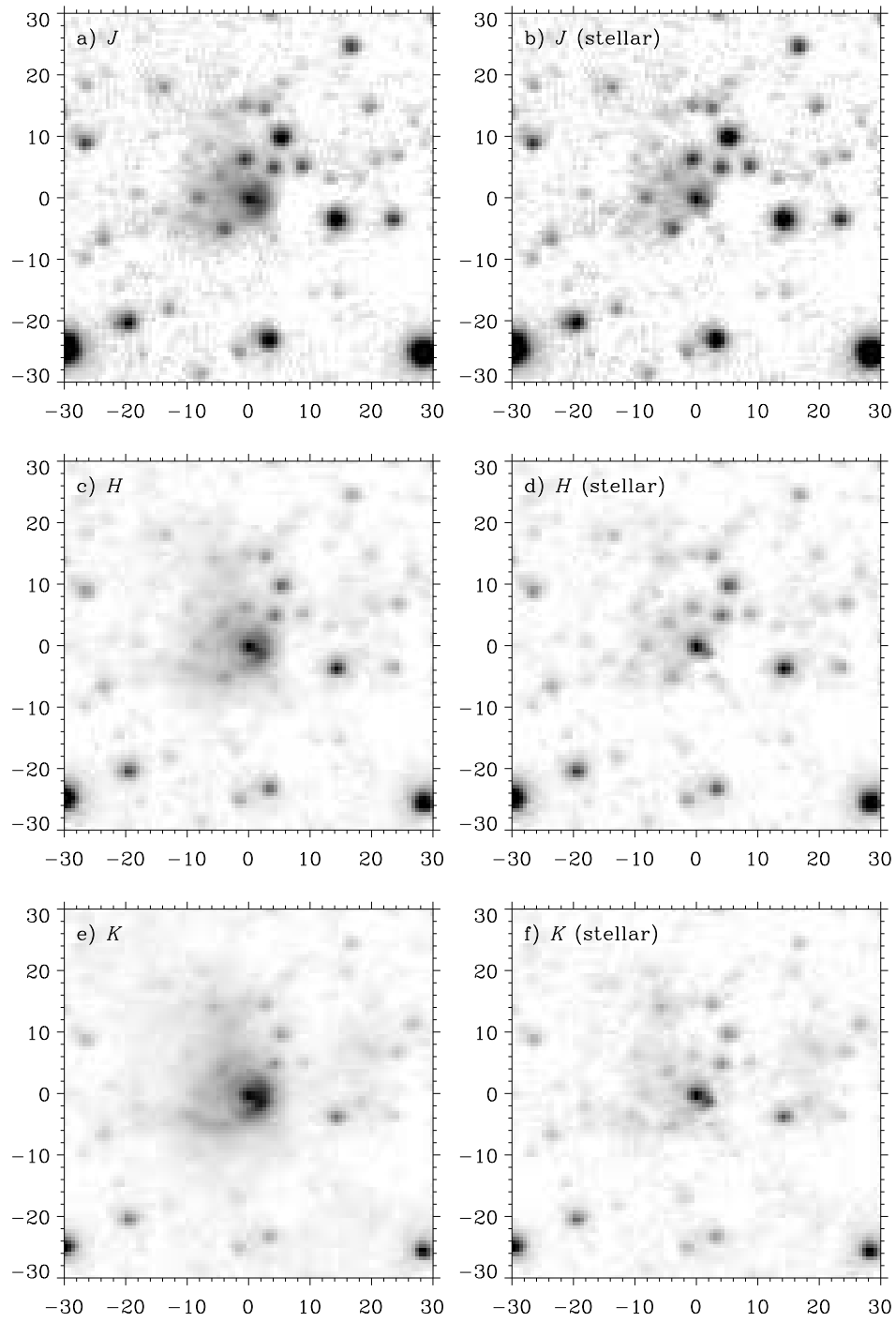


Fig. 9

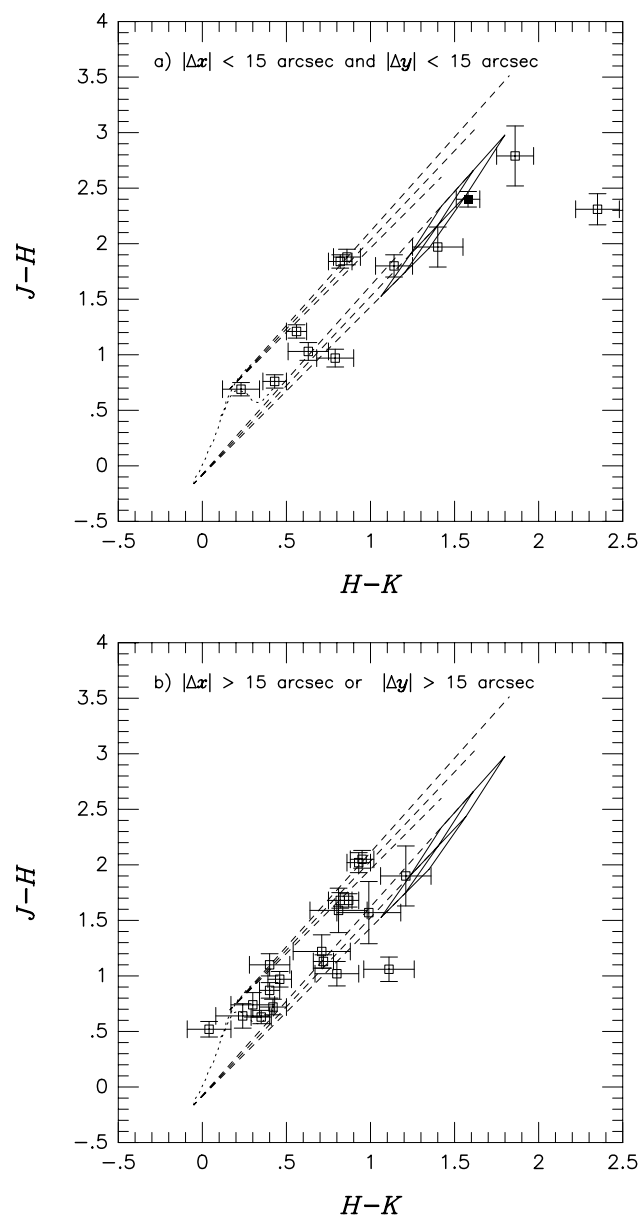


Fig. 10

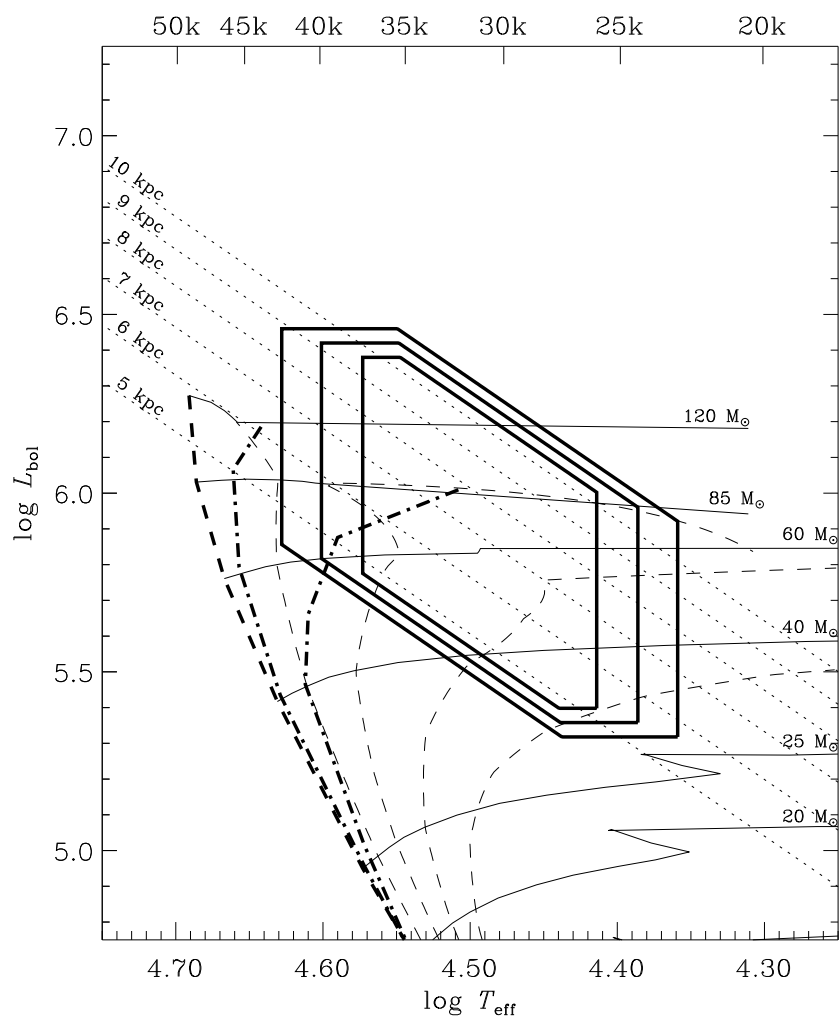


Fig. 11

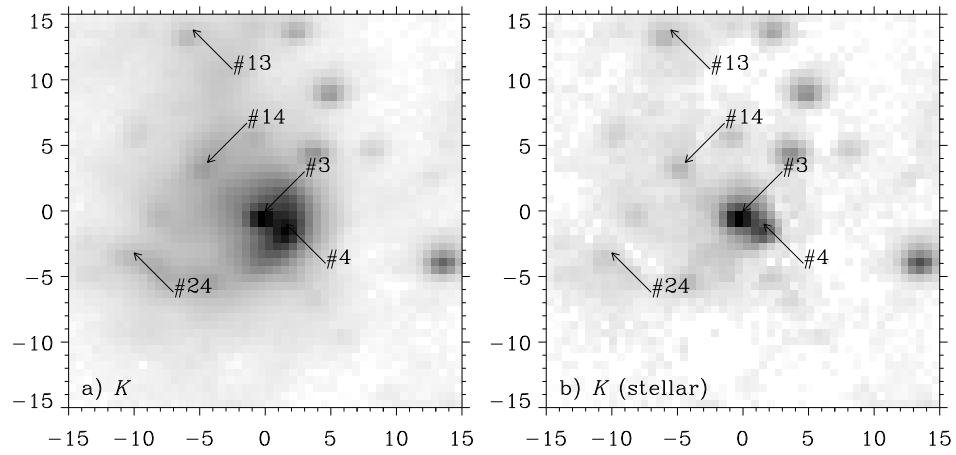


Table Captions

Table 1: Radio Data

Table 2: Spectral Energy Distribution

Table 3: Stellar Photometry

Table 1. Radio Data

Authors	Frequency	Telescope	Beam arcsec	LAS arcsec
Fey et al. (1995)	14.9 GHz/2 cm	VLA B+C+D	0.6×0.5	90
Cesaroni et al. (1994)	24.1 GHz/1.3 cm	VLA C+D	2.7×2.1	60
Afflerbach et al. (1994)	4.87 GHz/6 cm	VLA B	1.8×1.5	40
Claussen & Hofner (1996)	1.43 GHz/21 cm	VLA A	1.3×1.5	40
Hofner et al. (1996)	110 GHz/2.7 mm	OVRO	3.8×5.4	20

Table 2. Spectral Energy Distribution

Wavelength	F_ν Jy	Reference
21 cm	0.94	Claussen & Hofner (1996)
6 cm	3.18	Afflerbach et al. (1994)
2 cm	3.9	Fey et al. (1995)
1.3 cm	3.53	Cesaroni et al. (1994)
7 mm	2.85	Wood et al. (1988)
2.7 mm	2.37	Hofner et al. (1997)
1.3 mm	15.6 ^a	Mooney et al. (1995)
1.3 mm	8.0	Chini et al. (1986)
1.3 mm	5.81 ^b	Mooney et al. (1995)
790 μm	5.1×10^2	Hunter (1997)
350 μm	3.0×10^1	Hunter (1997)
100 μm	1.15×10^4	IRAS PSC
60 μm	7.50×10^3	IRAS PSC
25 μm	1.70×10^3	IRAS PSC
13.0 μm	2.13×10^2	Ball et al. (1996)
12 μm	2.17×10^2	IRAS PSC
12.6 μm	1.84×10^2	Ball et al. (1996)
12.0 μm	1.57×10^2	Ball et al. (1996)
9.7 μm	4.84×10^1	Ball et al. (1996)
8.5 μm	4.30×10^1	Ball et al. (1996)
5.0 μm	5.0	Herter et al. (1981)
3.8 μm	1.9	Herter et al. (1981)
2.2 μm	4.40×10^{-1}	This work
1.65 μm	9.48×10^{-2}	This work
1.25 μm	1.66×10^{-2}	This work

^aIntegrated flux

^b12 arcsec FWHM point source

Table 3. Stellar Photometry

Star	Δx arcsec	Δy arcsec	$J-H$	$H-K$	K
1	-28.9	-23.9	+0.87 \pm 0.05	+0.41 \pm 0.05	9.61 \pm 0.04
2	+27.4	-24.6	+0.98 \pm 0.06	+0.47 \pm 0.06	10.12 \pm 0.04
3	+0.0	+0.0	+2.40 \pm 0.05	+1.59 \pm 0.05	10.36 \pm 0.04
4	+1.6	-1.0	+2.28 \pm 0.11	+2.34 \pm 0.07	11.14 \pm 0.05
5	+13.8	-3.4	+1.22 \pm 0.05	+0.57 \pm 0.05	11.41 \pm 0.03
6	-18.8	-19.5	+1.68 \pm 0.05	+0.89 \pm 0.04	11.55 \pm 0.03
7	+3.9	+4.8	+1.84 \pm 0.05	+0.83 \pm 0.05	12.34 \pm 0.04
8	+5.1	+9.5	+0.76 \pm 0.05	+0.44 \pm 0.05	12.35 \pm 0.04
9	+3.2	-22.3	+0.63 \pm 0.04	+0.37 \pm 0.05	12.46 \pm 0.03
10	+2.5	+14.3	+1.89 \pm 0.06	+0.86 \pm 0.06	12.92 \pm 0.05
11	-25.6	+8.7	+1.13 \pm 0.05	+0.74 \pm 0.05	12.93 \pm 0.03
12	-1.4	-24.0	+2.02 \pm 0.08	+0.95 \pm 0.06	13.10 \pm 0.04
13	-5.5	+13.8	+2.79 \pm 0.26	+1.86 \pm 0.09	13.20 \pm 0.05
14	-4.4	+3.7	+1.80 \pm 0.09	+1.15 \pm 0.08	13.23 \pm 0.06
15	-3.8	-4.8	+0.98 \pm 0.06	+0.79 \pm 0.08	13.41 \pm 0.06
16	+23.4	+6.7	+2.04 \pm 0.07	+0.97 \pm 0.06	13.42 \pm 0.05
17	-22.9	-6.3	+1.69 \pm 0.06	+0.83 \pm 0.06	13.47 \pm 0.05
18	-2.4	+1.1	+1.34 \pm 0.15	+1.66 \pm 0.14	13.56 \pm 0.11
19	+16.2	+23.9	+0.72 \pm 0.06	+0.44 \pm 0.07	13.61 \pm 0.05
20	-2.3	-2.9	+1.92 \pm 0.22	+1.80 \pm 0.17	13.68 \pm 0.13

Table 3—Continued

Star	Δx arcsec	Δy arcsec	$J-H$	$H-K$	K
21	+17.6	-1.1	+2.28 ± 0.38	+2.18 ± 0.21	13.68 ± 0.09
22	+18.8	+7.2	+2.84 ± 0.41	+2.07 ± 0.11	13.75 ± 0.08
23	-0.6	+6.1	+0.70 ± 0.05	+0.23 ± 0.09	13.79 ± 0.08
24	-10.0	-3.2	+1.97 ± 0.17	+1.39 ± 0.13	13.93 ± 0.10
25	+22.7	-3.3	+0.52 ± 0.06	+0.08 ± 0.12	14.01 ± 0.11
26	-7.8	+0.1	+1.04 ± 0.07	+0.62 ± 0.11	14.03 ± 0.10
27	-29.3	+13.4	+1.38 ± 0.08	+0.83 ± 0.07	14.06 ± 0.05
28	-17.6	-1.9	+1.14 ± 0.40	+2.90 ± 0.27	14.25 ± 0.08
29	+15.3	+19.2	+1.58 ± 0.33	+1.84 ± 0.20	14.36 ± 0.08
30	+29.5	+28.5	+0.95 ± 0.09	+0.48 ± 0.09	14.41 ± 0.07
31	+8.4	+5.1	+0.79 ± 0.06	-0.03 ± 0.17	14.48 ± 0.16
32	-9.4	+6.2	+2.25 ± 0.22	+0.95 ± 0.16	14.49 ± 0.14
33	+3.5	+29.0	+1.01 ± 0.11	+0.82 ± 0.12	14.49 ± 0.10
34	-13.2	+17.5	+1.11 ± 0.09	+0.42 ± 0.12	14.53 ± 0.10
35	+20.0	+6.0	+1.07 ± 0.10	+1.13 ± 0.14	14.56 ± 0.12
36	-20.3	-13.8	+1.89 ± 0.26	+1.23 ± 0.15	14.83 ± 0.10
37	+29.1	+1.3	+1.36 ± 0.11	+0.72 ± 0.11	14.83 ± 0.08
38	-26.4	+23.2	+2.36 ± 0.53	+1.43 ± 0.18	14.87 ± 0.11
39	-27.3	+10.1	+1.58 ± 0.19	+0.85 ± 0.16	14.91 ± 0.12
40	+0.7	-22.0	+1.48 ± 0.26	+1.06 ± 0.18	14.94 ± 0.12

Table 3—Continued

Star	Δx arcsec	Δy arcsec	$J-H$	$H-K$	K
41	-12.4	-17.3	$+0.74 \pm 0.10$	$+0.32 \pm 0.13$	14.98 ± 0.10
42	-25.9	-9.3	$+1.23 \pm 0.15$	$+0.73 \pm 0.16$	15.01 ± 0.13
43	+19.1	+14.4	$+0.64 \pm 0.10$	$+0.26 \pm 0.16$	15.06 ± 0.13
44	-0.6	+14.6	$+0.90 \pm 0.10$	$+0.03 \pm 0.29$	15.24 ± 0.28
45	-20.5	-19.7	$+0.70 \pm 0.12$	$+0.18 \pm 0.24$	15.34 ± 0.22
46	-7.6	-27.4	$+0.62 \pm 0.12$	$+0.28 \pm 0.19$	15.42 ± 0.17
47	-17.6	+1.1	$+1.15 \pm 0.11$	$+0.34 \pm 0.26$	15.52 ± 0.25
48	+14.2	-14.5	$+1.20 \pm 0.12$	$+0.35 \pm 0.20$	15.53 ± 0.18
49	+3.9	-6.2	$+2.10 \pm 0.34$	$+0.48 \pm 0.43$	15.60 ± 0.41
50	-21.5	-17.9	$+1.61 \pm 0.45$	$+1.22 \pm 0.28$	15.61 ± 0.19
51	-25.6	+17.8	$+0.70 \pm 0.11$	$+0.14 \pm 0.20$	15.65 ± 0.17